Journal of the Brazilian Society of Mechanical Sciences and Engineering (2018) 40:427
https://doi.org/10.1007/s40430-018-1347-6

TECHNICAL PAPER

Finite element modeling and analysis of an atomic force microscope cantilever beam coupled to a piezoceramic base actuator

Kleber S. Rodrigues[1] · Marcelo A. Trindade[1]

Received: 23 January 2018 / Accepted: 9 August 2018 / Published online: 17 August 2018

Abstract
Characterization and analysis of sample surfaces with nanometer order topologies is essential to study properties such as roughness, resistance, molecular arrangements, failure, among others. Therefore, in recent decades, atomic force microscope (AFM) has become an essential tool, since it has the ability to get 3D nanometer order images of surfaces from some predefined kind of interaction. In order to understand the dynamics and improve the operation of base-cantilever-tip-sample AFM systems, several mathematical models were proposed in the literature. However, it seems that there is still a need of representative and parametric models able to capture material and geometric properties of the cantilever beam and piezoceramic base actuator. Hence, this work focuses on the development and analysis of a parametric model capable of properly representing the dynamics of an AFM cantilever beam when subjected to realistic operation conditions, using a finite element model for the cantilever beam and accounting for translational and rotational inertia of the probe tip and for the piezoceramic actuator that excites and controls the beam motion. All material and geometrical properties for the system (cantilever beam, probe tip and piezoceramic actuator) can be parametrized. Experimental SEM images and frequency responses of a real AFM cantilever beam are used to verify the model and also to define its parameters with very satisfactory results. A dynamic analysis of the cantilever beam when subjected to tip-sample nonlinear interaction forces is performed to develop a proper reduced-order model. The interaction forces were modeled using Lennard Jones potentials. Then, an analysis of the dynamic response of the cantilever beam for varying tip-sample initial distances is performed. Besides the appearance of the expected nonlinear behavior due to the tip-sample interaction forces, it is observed that the closer the sample is to the beam tip, the smaller is the tip displacement amplitude. Based on this observation, an analysis is performed to assess the correlation between the tip displacement and the surface topology of a diamond sample with satisfactory results.

Keywords Atomic force microscopy · Finite element method · Piezoceramic actuator · Cantilever beam · Atomic interaction forces

1 Introduction

In Physics, Biology, Engineering and many others branches of science, the nanoscale science is present studying how nanosized particles properties are different from those of large particles of the same substance [1]. It is also important to understand phenomena such as the interactions between prostheses and bones in medicine, catalysis of chemical reactions in industry, interactions between a surface and the external environment, exchange of electrons between neighboring atoms, their distribution and the chemical substances between them [2]. For that, the characterization and analysis of sample surfaces is essential to study properties such as roughness, resistance, molecular arrangements, failure, among others.

Before the invention of the scanning tunneling microscope (STM) [3], this kind of analyses was not experimentally possible. The invention of the STM opened a new area in the microscopy field, namely scanning probe microscopy, from which the atomic force microscope

Technical Editor: Wallace Moreira Bessa.

✉ Marcelo A. Trindade
trindade@sc.usp.br

[1] Department of Mechanical Engineering, São Carlos School of Engineering, University of São Paulo, São Carlos 13566-590, Brazil

(AFM) is one of its most important tools. From this point of view, the AFM working process has become a topic widely studied in recent years [4, 5]. As shown in Fig. 1, in an AFM system, the deflected tip of a flexible cantilever beam reflects a laser beam that is detected by a photo-detector. The position in which the laser beam gets to the photo-detector follows the deflection of the cantilever beam, which depends on the interaction between a probe tip on the cantilever beam and the sample being analyzed. The vibration amplitude of the cantilever beam, as measured by the photo-detector, is then compared to a reference value by a feedback control system that corrects the z-direction position of the base such that the cantilever beam deflection matches the reference value. The displacement of base can then be considered as a measure of the height of the sample surface at that point, relative to a reference value. By scanning the sample surface point-by-point with this technique, it is then possible to identify the topography of the sample surface.

In order to understand the dynamics and improve the operation of base-cantilever-tip-sample AFM systems, several mathematical models have been proposed in the literature to represent the system composed of cantilever beam, probe tip and base excitation. Most of these models, however, consider a system with one or two degrees-of-freedom, using 1 or 2-dof spring-mass-damper system [6–10] and focus mainly on the study of the tip dynamics. A disadvantage of this approach is that material and geometric properties of the cantilever beam and piezoceramic base actuator, which are highly coupled to the tip motion, are not easily accounted for. According to [11], modeling and analysis of the AFM system is essential to improve its operation. Another approach is to use continuous beam models to represent the AFM cantilever beam, considering Bernoulli–Euler [12–14] and Timoshenko [15, 16] assumptions. Some of the disadvantages of these previous approaches are that more complex beam geometries and boundary conditions are not accounted for and it is more difficult to perform parametric analysis and design. Some recent research works put forward the need of a finite element-based model, for different reasons, to enable their analyses of an AFM system [17–20]. It becomes clear that the added representativeness possibly brought by a finite element model may increase significantly the computational cost of the dynamic analysis. This is particularly important, since one of the important characteristics of the AFM system is the nonlinear interaction between probe tip and sample surface, which leads by itself to more expensive analysis.

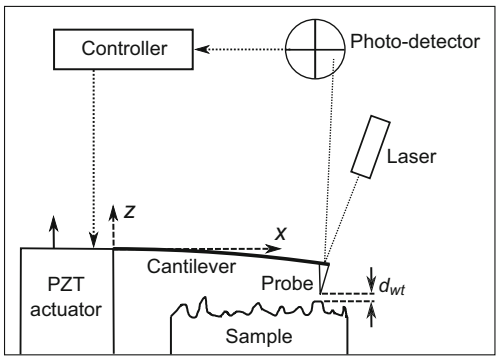

Fig. 1 Schematic representation of an AFM system (not in scale)

This work focuses on the development and analysis of a parametric model capable of properly representing the dynamics of an AFM cantilever beam when subjected to realistic operation conditions. For that, a finite element model for the cantilever beam is proposed, based on Bernoulli–Euler assumptions, which accounts for translational and rotational inertia of the probe tip, on one end (tip), and for the piezoceramic actuator that excites and controls the beam motion, on the other end (base). In order to verify the model and also to define its parameters, experimental scanning electron microscopy (SEM) images and frequency responses of a real AFM cantilever beam are used. Then, a reduced-order model was proposed and analyzed aiming at reducing computational cost of subsequent analyses. The minimum number of vibration modes to be retained in the reduced model is determined based on dynamic analyses of a cantilever beam subjected to nonlinear tip-sample interaction forces, which are modeled using Lennard Jones potentials. Then, the dynamic response of the cantilever beam for varying tip-sample initial distances is analyzed. This study adds value to the understanding and parametrization of the system dynamics, which could help finding better operating conditions for a given system (cantilever beam, probe tip, piezoceramic actuator and sample to be analyzed).

2 Mathematical modeling

In this section, a mathematical model to represent the dynamics of the AFM system, composed of a cantilever beam, clamped to a piezoceramic actuator at its left end and free at its right end, is presented. At the clamped end ($x = 0$), a piezoelectric ceramic actuator, responsible for the cantilever beam motion in z-direction, is considered. At the free end ($x = L$), a tip mass, representing the probe tip, and a point transversal force, representing the interaction between probe and sample surface, are considered (Fig. 1).

The AFM cantilever beam is modeled using a standard Bernoulli–Euler beam finite element model. The probe tip is represented by a mass m_t and rotary inertia I_t at the beam free end. At the clamped end, it is considered that the cantilever beam is perfectly coupled with the piezoceramic

actuator. The cantilever beam is considered to be homogeneous and uniform with length L_s, width b_s, thickness h_s, cross-sectional area and second moment of area, A_s and I_s, and made of an isotropic material with Young's modulus E_s, Poisson's ratio v_s and mass density ρ_s. The piezoceramic actuator is considered to be a homogeneous and uniform disk with thickness h_p and radius r_p, and made of PZT-5H transversally isotropic material (Lead Zirconate Titanate, Navy Type VI) with elastic stiffness coefficient $c^E_{p_{33}}$, piezoelectric coefficient $e_{p_{33}}$ and dielectric coefficient $\epsilon^{\varepsilon}_{p_{33}}$. At the free end, an interaction force f_t, represented by Lennard Jones Potentials is also considered. The probe tip is initially set at an initial distance d from the sample surface.

2.1 Finite element modeling of the cantilever beam

Considering the standard Bernoulli–Euler hypotheses for a slender beam in xz plane deflection, the displacements field may be written as

$$\overline{u}(x,y,z,t) = -zw'(x,t),\ \overline{v}(x,y,z,t) = 0,\ \overline{w}(x,y,z,t) = w(x,t), \tag{1}$$

where w is the transverse displacement (in z-direction) and $w' = \partial w/\partial x$ is the cross-sectional rotation angle.

Based on these kinematic hypotheses, the only non-null mechanical strain, that is the normal longitudinal strain ε_{s_1}, can be written from the usual strain-displacement relation as

$$\varepsilon_{s_1} = \partial\overline{u}/\partial x = -zw''. \tag{2}$$

Hermite cubic shape functions are assumed for the discretization of the transverse deflection $w(x, t)$, along the element length L_{se}, such that a two-node finite element with two degrees-of-freedom (dof) per node, namely deflection w_i and cross-sectional rotation angle w'_i $(i = 1, 2)$, is obtained as shown in Fig. 2. The elementary dof column vector $\mathbf{u}_e$ is defined as

$$\mathbf{u}_e = [\, w_1 \quad w'_1 \quad w_2 \quad w'_2 \,]^{\mathrm{t}}, \tag{3}$$

and the transverse displacement of the cantilever beam can be written in terms of the elementary dof as

$$w(x,t) = \mathbf{N}_s(x)\mathbf{u}_e(t). \tag{4}$$

Using (2), the normal strain can be discretized and written in terms of the elementary dof as

$$\varepsilon_{s_1} = -z\mathbf{B}_s\mathbf{u}_e, \text{ with } \mathbf{B}_{\mathrm{s}} = \mathbf{N}''_{\mathrm{s}}. \tag{5}$$

The virtual variation of kinetic and potential energies may be written in terms of the elementary nodal dof vector such that

$$\int \delta T_{se}\,\mathrm{d}t = -\int \delta\mathbf{u}_e^{\mathrm{t}}\mathbf{M}_{se}\ddot{\mathbf{u}}_e\,\mathrm{d}t, \quad \delta U_{se} = \delta\mathbf{u}_e^{\mathrm{t}}\mathbf{K}_{se}\mathbf{u}_e, \tag{6}$$

where $\mathbf{M}_{se}$ and $\mathbf{K}_{se}$ are the elementary mass and stiffness matrices of the cantilever beam defined by

$$\mathbf{M}_{se} = \int_0^{L_{se}} \rho_s A_s \mathbf{N}_s^{\mathrm{t}}\mathbf{N}_s\,\mathrm{d}x \quad \text{and} \quad \mathbf{K}_{\mathrm{se}} = \int_0^{\mathrm{L_{se}}} \mathrm{E_s I_s}\mathbf{B}_{\mathrm{s}}^{\mathrm{t}}\mathbf{B}_{\mathrm{s}}\,\mathrm{dx}. \tag{7}$$

Assembling all finite elements along the beam length, it is possible to write a global dof vector $\mathbf{u}$, such that total virtual variation of kinetic and potential energies are written as

$$\int \delta T_s\,\mathrm{d}t = -\int \delta\mathbf{u}^{\mathrm{t}}\mathbf{M}_s\ddot{\mathbf{u}}\,\mathrm{d}t, \quad \delta U_s = \delta\mathbf{u}^{\mathrm{t}}\mathbf{K}_s\mathbf{u}, \tag{8}$$

where $\mathbf{M}_s$ and $\mathbf{K}_s$ are the global mass and stiffness matrices.

At $x = L_s$, the cantilever beam is considered free to move but with actuation of interaction forces that will be properly modeled in the next section. At $x = 0$, a sliding-free boundary condition with $w'(0, t) = 0$ is considered for the beam. Later on, the left-end transversal displacement $w(0, t)$ will be set as coincident to the PZT actuator longitudinal displacement $u_p(t)$. Figure 3 shows a schematic representation of the cantilever beam coupled to the PZT actuator in the clamped end.

2.2 Modeling of probe tip inertia and interaction forces

To account for the probe tip inertia at the free end of the cantilever beam, the deflection $w(L_s, t)$ and cross-sectional rotation angle $w'(L_s, t)$ of the beam tip are written as function of the global dof vector, so that

Fig. 2 Two-node/four-dof Bernoulli–Euler beam finite element

Fig. 3 Schematic representation of the cantilever beam coupled to a PZT actuator (not in scale)

$$w(L_s,t) = \mathbf{L}_w\mathbf{u},\ w'(L_s,t) = \mathbf{L}_{wx}\mathbf{u} \text{ with}$$
$$\mathbf{L}_w = [0 \quad \cdots \quad 0 \quad 1 \quad 0],\ \mathbf{L}_{wx} = [0 \quad \cdots \quad 0 \quad 1]. \tag{9}$$

Substituting the last equation into the virtual variation of translational and rotational kinetic energies of the probe tip and defining m_t and I_t as the mass and rotation inertia of the probe tip, respectively, leads to an equivalent mass matrix $\mathbf{M}_t$ to be added to the mass matrix of the cantilever beam. The mass matrix $\mathbf{M}_t$ is written as

$$\mathbf{M}_t = \mathbf{L}_w^{\mathrm{t}} m_t \mathbf{L}_w + \mathbf{L}_{wx}^{\mathrm{t}} I_t \mathbf{L}_{wx}. \tag{10}$$

Hence, the total mass matrix of the cantilever beam, including probe tip inertia, is defined as $\mathbf{M}_{st} = \mathbf{M}_s + \mathbf{M}_t$. The probe tip is subjected to attraction and repulsion atomic forces due to the interaction between probe tip and sample surface. This transversal force, defined as f_t, is accounted for in the finite element model through its contribution to the virtual work done by external forces, that reads

$$\delta W = \delta w(L_s,t) f_t = \delta \mathbf{u}^{\mathrm{t}} \mathbf{F}_t, \tag{11}$$

where the vector of nodal forces corresponding to the tip-sample interaction forces is $\mathbf{F}_t = \mathbf{L}_w^{\mathrm{t}} f_t$.

In this work, the tip-sample interaction forces f_t are modeled using Lennard Jones potentials, which describes the potential energy of the interaction between two molecules or atoms accounting for attraction forces (dipole–dipole, induced dipole–dipole, London interactions) and repulsion forces. The model assumes that, as the distance between the two entities diminishes, attraction forces are induced up to an equilibrium distance, such that, for smaller distances, repulsion forces overcome attraction ones inducing the separation of the entities.

The interaction force f_t is then written in terms of the distance between tip and sample nearest atoms and also physical and geometrical properties of tip and sample. According to [21], it may be written as

$$f_t = \frac{H_1 R_t}{180(d + w_t)^8} - \frac{H_2 R_t}{6(d + w_t)^2}, \tag{12}$$

where d is the distance between probe tip and sample surface for undeformed cantilever beam and $w_t = w(L_s,t)$ is the tip transversal displacement (defined as positive when moving away from the sample). H_1 and H_2 are the Hamaker constants for the attractive and repulsive potentials and R_t is the probe tip radius [12]. Figure 4 shows graphically the interaction force in terms of the tip-sample distance $(d + w_t)$ using parameters H_1, H_2 and R_t taken from [12] and shown in Table 1.

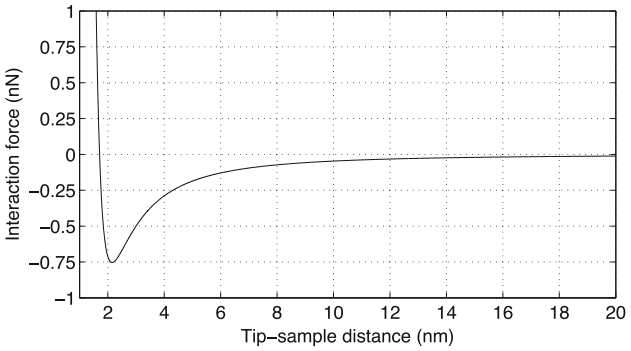

Fig. 4 Tip-sample interaction force in terms of tip-sample distance using Lennard Jones Potentials

Table 1 Known material parameters and estimated geometrical parameters based on SEM images for a real AFM cantilever

Parameter	Symbol	Value	Unit
Cantilever beam			
Length	L_s	127	μm
Width	b_s	33	μm
Thickness	h_s	3.37	μm
Young Modulus	E_s	176×10^9	N m^{-2}
Mass density	ρ_s	2330	kg m^{-3}
Probe tip			
Tip radius	R_t	150	nm
Base radius	r_t	11.6	μm
Height	h_t	17.4	μm
Mass	m_t	5.6×10^{-12}	kg
Rotation inertia	I_t	23.4×10^{-22}	kg m^2
Repulsive Hammaker constant	H_1	1.3956×10^{-70}	J m^6
Attractive Hammaker constant	H_2	1.865×10^{-19}	J
PZT disk			
Thickness	h_p	2	mm
Radius	R_p	15	mm
Piezoelectric coefficient	$e_{p_{33}}$	23.3	C m^{-2}
Elastic coefficient	$c^E_{p_{33}}$	4.8309×10^{10}	N m^{-2}
Dielectric coefficient	$\epsilon^{\varepsilon}_{p_{33}}$	1.3×10^{-8}	F m^{-1}
Mass density	ρ_p	7500	kg m^{-3}

2.3 Modeling of piezoceramic base actuator

The PZT piezoceramic actuator is modeled considering a unidimensional longitudinal deformation (in z-direction). The internal (potential) energy U_p of the actuator is represented by its electric enthalpy H, written in terms of the normal longitudinal elastic strain ε_{p_3} and longitudinal electric field E_{p_3}, such that

$$\delta U_p = \delta H(\varepsilon_{p_3}, D_{p_3}) = \delta\varepsilon_{p_3}\sigma_{p_3} - \delta E_{p_3} D_{p_3}, \tag{13}$$

combined to the following linear piezoelectric constitutive equations

$$\sigma_{p_3} = c^E_{p_{33}}\varepsilon_{p_3} - e_{p_{33}}E_{p_3}, \quad D_{p_3} = e_{p_{33}}\varepsilon_{p_3} + \epsilon^{\varepsilon}_{p_{33}}E_{p_3}, \tag{14}$$

where σ_{p_3} is the mechanical stress, D_{p_3} is the longitudinal electric displacement, $c^E_{p_{33}}$ is the effective elastic stiffness coefficient (at constant electric field), $e_{p_{33}}$ is the effective piezoelectric coefficient and $\epsilon^{\varepsilon}_{p_{33}}$ is the effective dielectric permittivity (at constant strain).

Thus, the virtual variation of potential energy for the PZT actuator may be written as

$$\begin{aligned}\delta U_p = \int \Big(& \delta\varepsilon_{p_3} c^E_{p_{33}}\varepsilon_{p_3} - \delta\varepsilon_{p_3} e_{p_{33}} E_{p_3} \\ & - \delta E_{p_3} e_{p_{33}}\varepsilon_{p_3} - \delta E_{p_3}\epsilon^{\varepsilon}_{p_{33}} E_{p_3}\Big)\,\mathrm{d}\Omega.\end{aligned} \tag{15}$$

Since the actuator thickness is much smaller than its diameter, uniform mechanical strain and electric fields along the longitudinal (thickness) direction are considered. Then, the longitudinal strain and electric field can be written, respectively, as $\varepsilon_{p_3} = u_p/h_p$ and $E_3 = V_p/h_p$, where u_p is the longitudinal displacement of the actuator at the end fixed to the cantilever beam, h_p is the actuator thickness and V_p is the electric voltage applied to the piezoceramic actuator.

Integration of (15) over the actuator's volume leads to

$$\delta U_p = \delta u_p k_{pm} u_p - \delta u_p k_{pp} V_p - \delta V_p k_{pp} u_p - \delta V_p k_{pe} V_p, \tag{16}$$

where $k_{pm} = c^E_{p_{33}} A_p/h_p$, $k_{pp} = e_{p_{33}} A_p/h_p$ and $k_{pe} = \epsilon^{\varepsilon}_{p_{33}} A_p/h_p$ are the effective elastic, piezoelectric and dielectric stiffnesses of the piezoceramic actuator.

Since, in this work, the piezoceramic disk will only serve as an actuator, it follows that the electric voltage V_p is prescribed, so that $\delta V_p = 0$, and, thus, the virtual variation of potential energy is simplified to

$$\delta U_p = \delta u_p k_{pm} u_p - \delta u_p k_{pp} V_p. \tag{17}$$

The virtual variation of the kinetic energy of the actuator is written as

$$\int \delta T_p\,\mathrm{d}t = -\int\int \delta\bar{u}_p \rho_p \ddot{\bar{u}}_p\,\mathrm{d}\Omega\,\mathrm{d}t, \tag{18}$$

Assuming that the actuator's longitudinal displacement in z-direction is $\bar{u}_p(z) = z u_p/h_p$ and integrating over the actuator volume yields

$$\int \delta T_p\,\mathrm{d}t = -\int \delta u_p \frac{m_p}{3}\ddot{u}_p\,\mathrm{d}t. \tag{19}$$

where $m_p = \rho_p A_p h_p$ is the mass of the piezoceramic actuator.

2.4 Equations of motion for the coupled system

Based on previous virtual variations of kinetic and potential energies and work done by external forces for the cantilever beam and the piezoceramic actuator, the extended Hamilton's principle for the coupled system may be written as

$$\int \left(\delta T_s + \delta T_p - \delta U_s - \delta U_p + \delta W\right)\mathrm{d}t = 0, \tag{20}$$

where δT_s and δU_s are defined in (8), δW is defined in (11) and δU_p and δT_p are defined in (17) and (19), respectively.

In order to couple the cantilever beam to the piezoceramic actuator, it is considered that the displacement of the cantilever beam at $x = 0$, $w(0, t)$, is equal to the displacement of the piezoceramic actuator upper surface, $u_p(t)$, such that $u_p(t) = w(0,t) = \mathbf{L}_p\mathbf{u}(t)$, where $\mathbf{L}_p = [1\ 0 \cdots\ 0]$. Then, substituting this expression of u_p in terms of $\mathbf{u}$ in (17) and (19), leads to

$$\delta U_p = \delta\mathbf{u}^{\mathrm{t}}\mathbf{K}_p\mathbf{u} - \delta\mathbf{u}^{\mathrm{t}}\mathbf{F}_p, \quad \int \delta T_p\,\mathrm{d}t = -\int \delta\mathbf{u}^{\mathrm{t}}\mathbf{M}_p\ddot{\mathbf{u}}\,\mathrm{d}t, \tag{21}$$

where $\mathbf{K}_p$ and $\mathbf{M}_p$ are the stiffness and mass matrices of the piezoceramic actuator and $\mathbf{F}_p$ is an equivalent electromechanical (piezoelectric) force vector due to electric voltage applied to the piezoceramic actuator, such that

$$\mathbf{K}_p = k_{pm}\mathbf{L}_p^{\mathrm{t}}\mathbf{L}_p, \ \mathbf{M}_p = (m_p/3)\mathbf{L}_p^{\mathrm{t}}\mathbf{L}_p, \ \mathbf{F}_p = \mathbf{L}_p^{\mathrm{t}} k_{pp} V_p. \tag{22}$$

Therefore, accounting for (21) in (20), leads to the following equations of motion for the coupled system

$$\mathbf{M}\ddot{\mathbf{u}} + \mathbf{D}\dot{\mathbf{u}} + \mathbf{K}\mathbf{u} = \mathbf{F}_t + \mathbf{F}_p, \tag{23}$$

where $\mathbf{M} = \mathbf{M}_{st} + \mathbf{M}_p$ and $\mathbf{K} = \mathbf{K}_s + \mathbf{K}_p$ are global mass and stiffness matrices for the coupled system (actuator/cantilever/probe). The two external force vectors $\mathbf{F}_t$ and $\mathbf{F}_p$ stand for the tip-sample interaction force and electromechanical force induced by the voltage applied to the actuator, respectively. In addition, a damping matrix $\mathbf{D}$ will be defined a posteriori to approximate all existing damping sources.

3 Model reduction, damping estimation and model validation

In order to reduce the computational cost of subsequent numerical analyses, a modal reduction is considered to reduce the system dimension. For that, an analysis was performed to evaluate the minimum number of vibration modes that are required in order to properly represent the system response under operational conditions. In addition, a model updating and validation was carried out using geometrical properties of a real AFM cantilever beam, including probe tip, obtained via scanning electron microscopy (SEM), and of piezoceramic actuators normally used in AFMs, and, also, frequency responses of the cantilever beam obtained from experimental tuning of a real AFM. These data were used to compare experimental and numerically predicted fundamental resonance frequency and damping factor and, therefore, to fine-tune model parameters and, thus, obtain a more representative model.

3.1 Model reduction using modal truncation

The reduced model is obtained by projecting the equations of motion of the coupled system into a reduced (truncated) modal basis. The modal basis is obtained considering the cantilever beam coupled to the piezoceramic actuator, but with no voltage applied, that is $\mathbf{F}_p = 0$, and without nonlinear interaction between tip and sample, that is $\mathbf{F}_t = 0$. An undamped modal basis is considered and, for that, the system damping is neglected at this point to yield real natural frequencies and vibration modes. Therefore, the following eigenvalue problem is considered

$$(-\omega_j^2\mathbf{M} + \mathbf{K})\boldsymbol{\phi}_j = 0, \text{with j} = 1, \ldots, \text{N}. \tag{24}$$

Then, the nodal displacements are written in terms of the corresponding modal coordinates related to the N first vibration modes, such that

$$\mathbf{u} \approx \sum_{j=1}^{N} \boldsymbol{\phi}_j q_j. \tag{25}$$

Considering a mass normalization of the eigenvectors $\boldsymbol{\phi}_j$, such that $\boldsymbol{\phi}_j^{\mathrm{t}}\mathbf{M}\boldsymbol{\phi}_j = 1$, the equations of motion projected onto the modal basis are written as

$$\ddot{q}_j + 2\xi_j\omega_j\dot{q}_j + \omega_j^2 q_j = \boldsymbol{\phi}_j^{\mathrm{t}}\mathbf{F}_t + \boldsymbol{\phi}_j^{\mathrm{t}}\mathbf{F}_p, \tag{26}$$

where the modal damping factors ξ_j were estimated from the experimentally obtained frequency response of a real AFM cantilever beam.

3.2 Damping estimation, parameters acquisition, model updating and model verification

In order to verify the proposed model, the material and geometrical properties as well as the resonance frequency and frequency response of a real cantilever was obtained in collaboration with the Thin Films Laboratory of the Institute of Physics of the University of São Paulo. Two different devices were used to perform this characterization, a nanoscope IIIa digital instruments atomic force microscope (AFM) and a Jeol 6460LV scanning electronic microscope (SEM). Using the AFM and performing the cantilever tuning with frequencies varying from 100 to 500 kHz, it was possible to obtain its resonant frequency response. Applying the half power bandwidth method (− 3 dB) in the frequency response, as shown in Fig. 5, it follows that $\omega_0 = 225.46$ kHz, $\omega_1 = 225.10$ kHz and $\omega_2 = 225.73$ kHz. Then, the modal damping factor ξ can be estimated as,

$$\xi = \frac{\omega_2 - \omega_1}{2\omega_0} = 0.0014. \tag{27}$$

Independently, the quality Q-factor of the cantilever beam is provided by the AFM as $Q = 358$ and, since $\xi = 1/2Q = 0.0014$, the cantilever beam damping factor is verified. Therefore, this damping factor value will be used in the following simulations.

On the other hand, with the help of SEM images, as shown in Figs. 6 and 7, the geometric properties of the cantilever beam and probe tip were estimated.

From the SEM images presented in Figs. 6 and 7, the cantilever beam was considered to have a uniform rectangular cross section and the probe tip was approximated as a uniform cone, both being made of a single piece of uniform material. Besides the geometric properties obtained from the SEM images, in order to fine-tune the experimentally

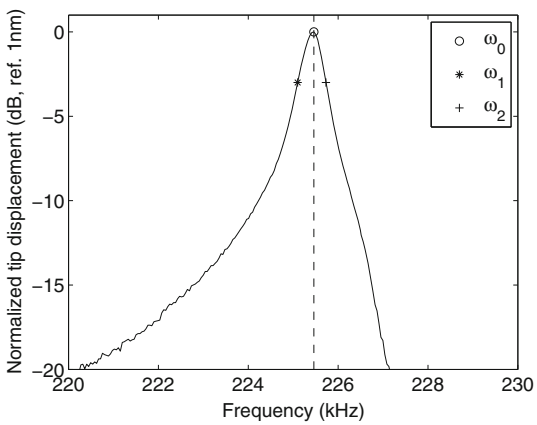

Fig. 5 Half power bandwidth method to estimate the equivalent damping factor

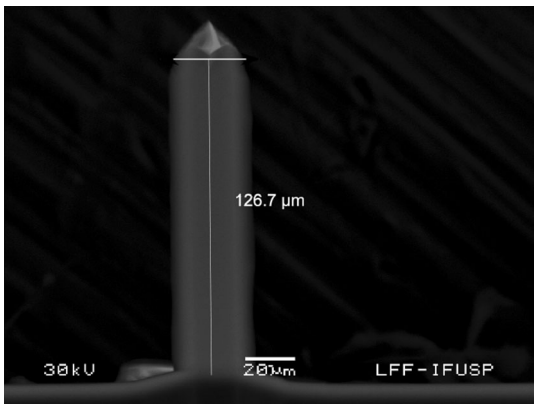

Fig. 6 Bottom view of SEM image of a real AFM cantilever beam

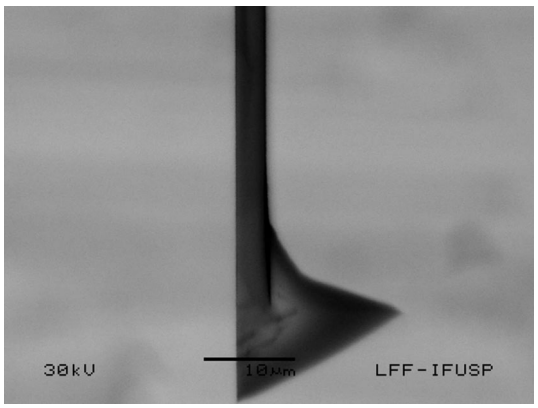

Fig. 7 Lateral view of SEM image, zoomed at the probe tip region, of a real AFM cantilever beam

obtained fundamental resonant frequency of the system, a numerical update of the tip cone base radius and height (r_t and h_t) and of the actuator disk's radius and height (r_p and h_p) was performed. The tip-sample interaction properties, H_1 and H_2, were taken from [12] and, along with other identified parameters, are shown in Table 1.

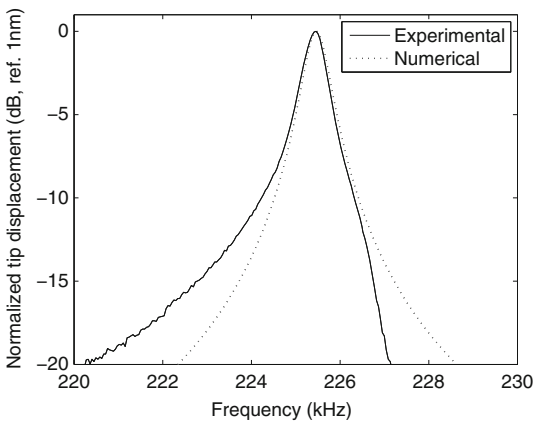

Fig. 8 Comparison between experimental data and numerical simulations

Figure 8 presents both experimental and numerical frequency responses, using the identified geometrical and material properties. It is possible to observe that the peaks are very similar, with nearly coincident resonance frequency. First, it was desired to match the resonance frequency, regardless of the bell shaped curve. The peak frequency obtained via experimental tuning of a real AFM was 225.46 kHz, and the peak frequency obtained via numerical simulation is 225.47 kHz, which means that the relative error between them is 0.0044%. It is then concluded that the considered geometric and material model parameters are representative of the studied real AFM and, therefore, they will be used in the following analyses.

3.3 Analysis of the minimum number of vibration modes to be retained in the reduced model

In this section, an analysis of the number of vibration modes that should be retained in a reduced-order model, in order to properly capture the dynamic behavior of the system, is performed. For that, an excitation through the PZT actuator, in the form of a sinusoidal applied electric voltage $V_p = \tilde{V}_p \sin(\omega t)$ with $\tilde{V}_p = 8.8V$ and $\omega = 202.92$ kHz is considered. These values of frequency and amplitude of the drive voltage were chosen to simulate real AFM operation, were excitation frequency is near the fundamental resonance and excitation amplitude is set based on a target tip free amplitude. In order to evaluate the need of a number of vibration modes when subjected to the nonlinear tip-sample interaction, the frequency response function of the probe tip displacement was evaluated for different tip-sample initial distances d. Notice that it is expected that the tip-sample interactions should increase by diminishing the tip-sample distances.

Figure 9 shows the frequency responses of the probe tip for different tip-sample initial distances ($d = \{90, 88, 84, 63\}$ nm) and when considering increasing number of vibration modes retained in the reduced-order model. Since the system becomes nonlinear for smaller tip-sample initial distances, the frequency response was obtained using fast Fourier transform (FFT) of the time response under the sinusoidal excitation by the PZT actuator. It is noticeable that, within the frequency range considered (100–600 kHz), three peaks can be easily observed for the higher tip-sample distance, except for the model with only one vibration mode. The second and third peaks are due to the first and second resonance frequencies of the system, whereas the first peak is due to the excitation frequency. That is why, when considering only the first vibration mode in the reduced model, the third peak is not observed. Moreover, the more the tip-sample distance is

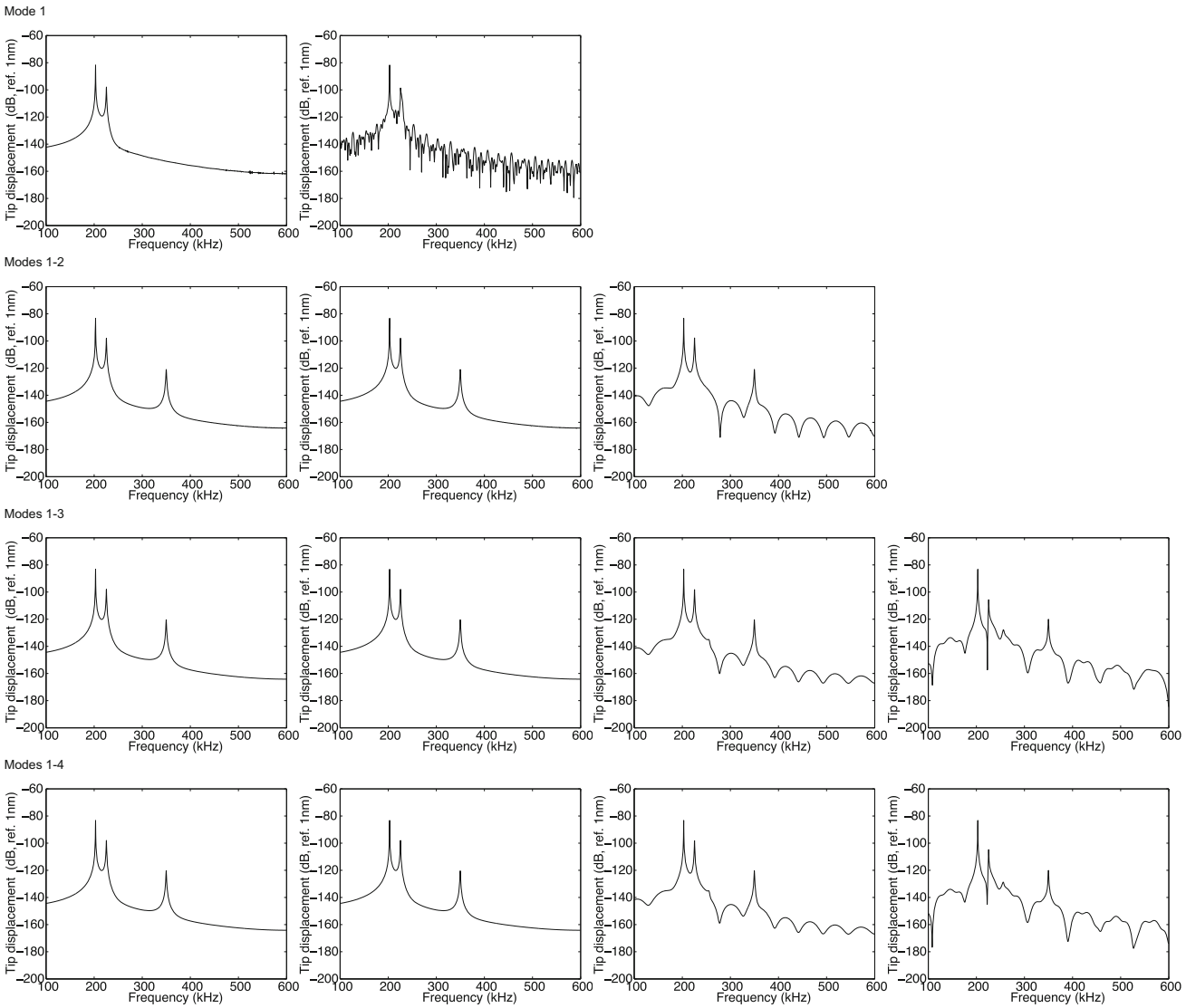

Fig. 9 Frequency responses of the probe tip under excitation through the PZT actuator for different tip-sample initial distances and when considering up to four vibration modes in the reduced-order model. From left to right: $d = \{90, 88, 84, 63\}$ nm

reduced, the more important becomes the nonlinear interaction between vibration modes, because of the increasing effect of the tip-sample interaction forces.

This leads to both a disturbance of the frequency response curves and also a modification of the displacement distribution along the beam span. For the latter reason, the reduced-order model with only the first vibration mode was not able to account for the local deformation of the beam tip and did not converge even for relative high tip-sample distances (88 nm). The same behavior was observed for the other reduced models, such that the two modes model stopped converging for tip-sample distances smaller than 84 nm, and the three modes model stop converging for tip-sample distances smaller than 63 nm. With four vibration modes, the model converged even for very low tip-sample distances (smaller than 1 nm), and, thus, it is suggested that a reduced-order model with the first four vibration modes is satisfactory and shall be used for following analyses.

4 Analyses of the coupled system response

4.1 Effect of tip-sample initial distance on the cantilever response

The goal of this section is to analyze the dynamic response of the cantilever beam when tip-sample initial distance d is diminished. Furthermore, it will be possible to observe the effect of the intermolecular tip-sample interaction forces on the system behavior.

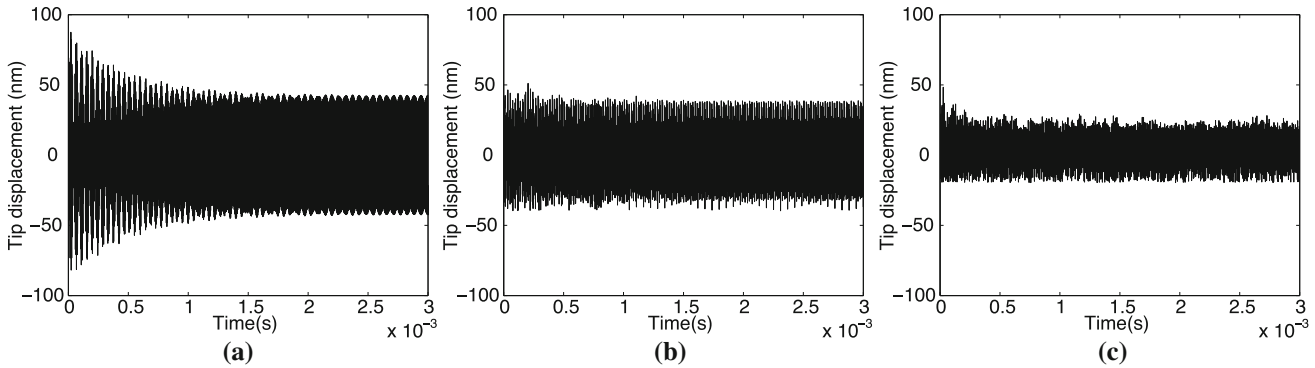

Fig. 10 Time response of the tip displacement using four-mode reduced model for different tip-sample initial distances. From left to right, $d = \{100, 40, 20\}$ nm

As shown in Fig. 10a, for tip-sample initial distances equal to, or higher than, $d = 100$ nm, in which cases the cantilever is considered to be free from the intermolecular forces, the cantilever beam tip displacement present maximum and minimum amplitudes of 87 and -82 nm, respectively, at the transient, given the considered sinusoidal base excitation amplitude. When in steady-state regime, the oscillation varies from -42 to 44 nm. By reducing the tip-sample initial distance to $d = 40$ nm (Fig. 10b) and $d = 20$ nm (Fig. 10c), it is possible to observe that the minimum amplitude is clearly constrained by the tip-sample initial distance. It is also noticeable that the maximum amplitude is also reduced and the transient higher amplitudes disappear faster. However, the steady-state response is much less uniform indicating the more important effects of the nonlinearities.

The tip-sample interaction forces for these three tip-sample initial distances are shown in Fig. 11. Since attraction and repulsion forces are of very different magnitudes, they are shown separately. However, it is their sum that acts on the cantilever beam tip and, thus, induces the nonlinearities observed in the tip displacement responses. For comparison purposes, the plot scales are the same for the three tip-sample initial distances. For $d = 100$ nm, small attraction forces are hardly noticeable during the transient regime, while repulsion forces are negligible (Fig. 11a). By decreasing the tip-sample initial distance to $d = 40$ nm (Fig. 11b) and $d = 20$ nm (Fig. 11c), these forces become clearly observable and not only during transient regime. Notice that repulsion forces are much higher, specially when the tip-sample distance decreases to very small values (smaller than 2 nm). Nevertheless, for small tip-sample initial distances, the attraction forces are always active and, thus, influencing the dynamic response of the cantilever.

For comparison purposes, Fig. 12 presents a compilation of all time histories as the tip-sample initial distance decreases. As previously observed, it is noticeable that while d decreases, the transient region disappears and the displacement amplitude gets smaller and unsymmetrical, with a flattening on the negative region, showing that the tip starts to get very close to the sample surface.

It is also worthwhile to analyze the effect of the tip-sample interaction forces on the frequency response of the cantilever beam tip. As in the previous section, this was done using FFT of the time responses shown in Fig. 10. Also as previously shown, for higher tip-sample initial distances ($d = 100$ nm, Fig. 13a), where tip-sample

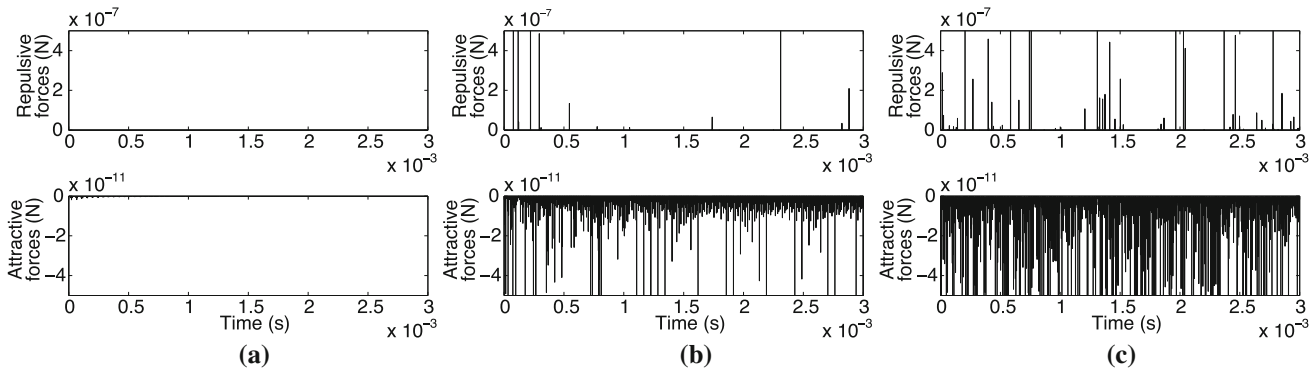

Fig. 11 Time response of the tip-sample attraction and repulsion forces for different tip-sample initial distances. From left to right, $d = \{100, 40, 20\}$ nm

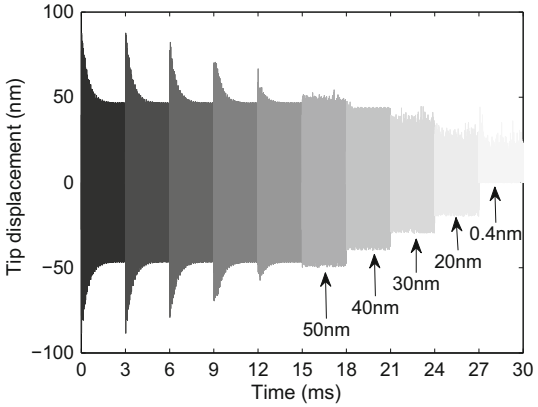

Fig. 12 Compilation of time responses of the probe tip displacement for different tip-sample initial distances

interaction forces are much smaller and, thus, negligible, three different peaks are clearly observed. The first being due to the excitation frequency and the others due to the first two resonant frequencies. As the tip-sample initial distance is diminished to $d = 40$ nm (Fig. 13b) and $d = 20$ nm (Fig. 13c), other peaks and distributed noise appear in the frequency response. The presence of multiple harmonics due to the nonlinearities suggests that it is important to account for more than one vibration mode (more than one degree-of-freedom) in the reduced-order model [22, 23]. For instance, for $d = 20$ nm, the only clear response peaks are due to excitation frequency and its multiples, which highlights the effect of interaction forces in the system behavior. A similar analysis was performed for other values of tip-sample initial distance and it is shown in Fig. 14.

4.2 Estimation of sample surface topology from cantilever tip amplitudes

In this section, it is proposed to use the time response of the cantilever beam tip amplitudes to estimate a sample surface topology. Although the intention is not to replicate the operation of a real AFM, since here there is no base repositioning feedback control, this analysis allows to check if there is enough correlation between tip amplitude response and tip-sample initial distance. For that, the analysis was based on a real topological surface of a diamond sample, shown in Fig. 15, that was obtained using the real AFM previously cited. The sample surface was scanned using 512×512 points of observation over the sample area of $150 \times 150\mu m^2$, leading to a point-to-point distance of 2.91 nm. In addition to the image, the data corresponding to the surface heights used to generate the topological image was also obtained and reset to heights ranging from -431 to 625 nm.

It is known that to obtain this image, among other things, the AFM device has used a feedback controller to maintain the cantilever tip amplitude oscillation constant, but, even without such control system, the main idea here is to reproduce a small area of the surface shown in Fig. 15 by performing point-to-point simulations using the reduced-order model proposed in this work. For that, a small region of the sample, represented by a mesh of 32×32 measurement points, was considered.

The considered simulation procedure is schematically represented in Fig. 16 and consisted on deducing the height of sample surface in a particular xy point, $z_{i,j}$, with $i \in [1, m]$ and $j \in [1, n]$ over the $m \times n$ measurement points, from a reference tip-sample initial distance, d. Notice that the scheme depicted in Fig. 16 is out of scale to allow observation of the variables involved, while the probe tip height may be more than 1000 times larger than the sample height. Then, the actual tip-sample initial distance to be considered in the simulations is defined as $d - z_{i,j}$. Therefore, when the cantilever is vibrating, the distance between the probe tip and sample surface may be written as

$$d_{wt} = d - z_{i,j} + w_t. \tag{28}$$

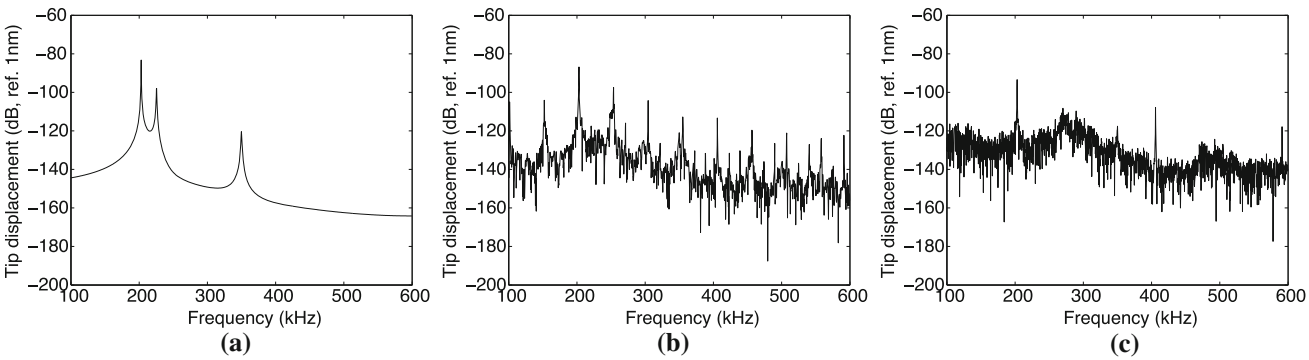

Fig. 13 Frequency response of the probe tip displacement calculated using four-mode reduced model for different tip-sample initial distances. From left to right, $d = \{100, 40, 20\}$ nm

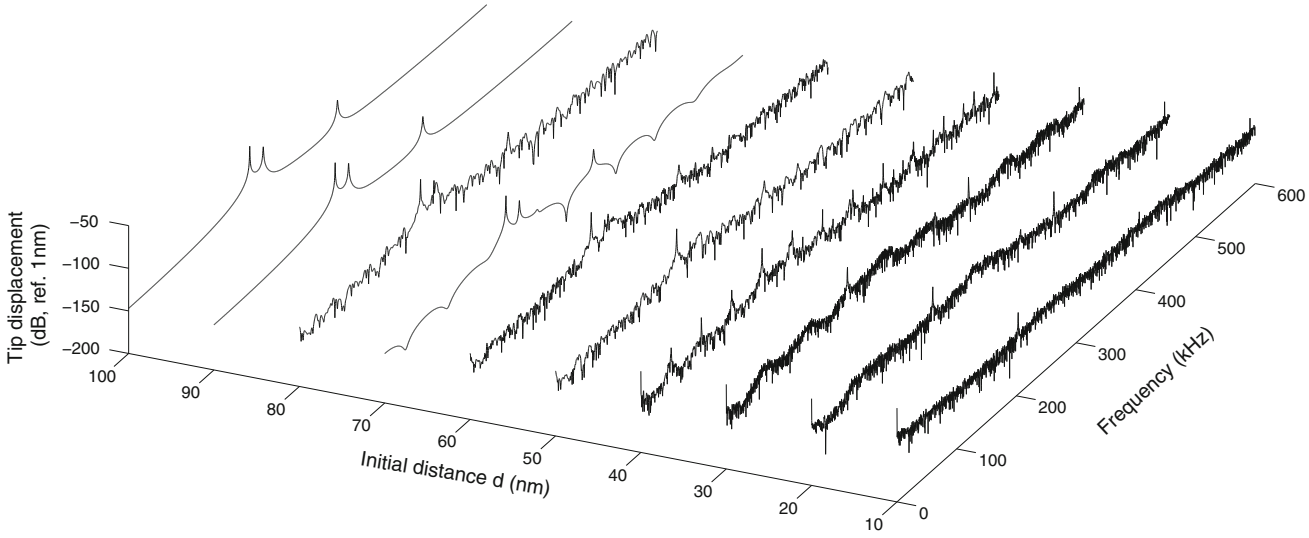

Fig. 14 Frequency response of the probe tip displacement for different tip-sample distances

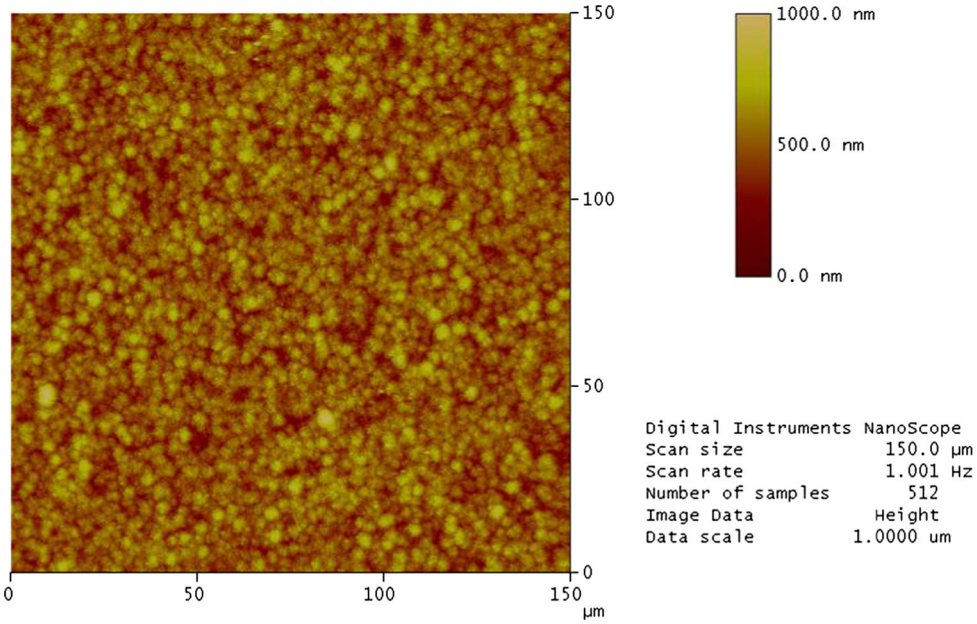

Fig. 15 Topological surface of a diamond sample obtained using a Nanoscope IIIa Digital Instruments AFM

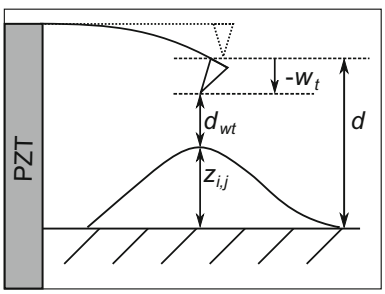

Fig. 16 Schematic representation of the procedure to obtain the sample topological surface (out of scale)

where w_t is the absolute tip deflection of the cantilever beam.

The small sample surface, covering an area of 87.89nm^2, considered in the present simulation is represented by a 32×32 matrix of surface heights ranging from -30 to 24 nm, depicted in Fig. 17a. For each one of the measurement points, a simulation was performed to obtain the time response of the cantilever beam tip considering a tip-sample initial distance of $d = 38.5$ nm, which was manually tuned to obtain a satisfactory topology characterization. As previously presented, the tip-sample initial distance was reduced by the height of the measurement point to simulate the presence of the cantilever tip over that

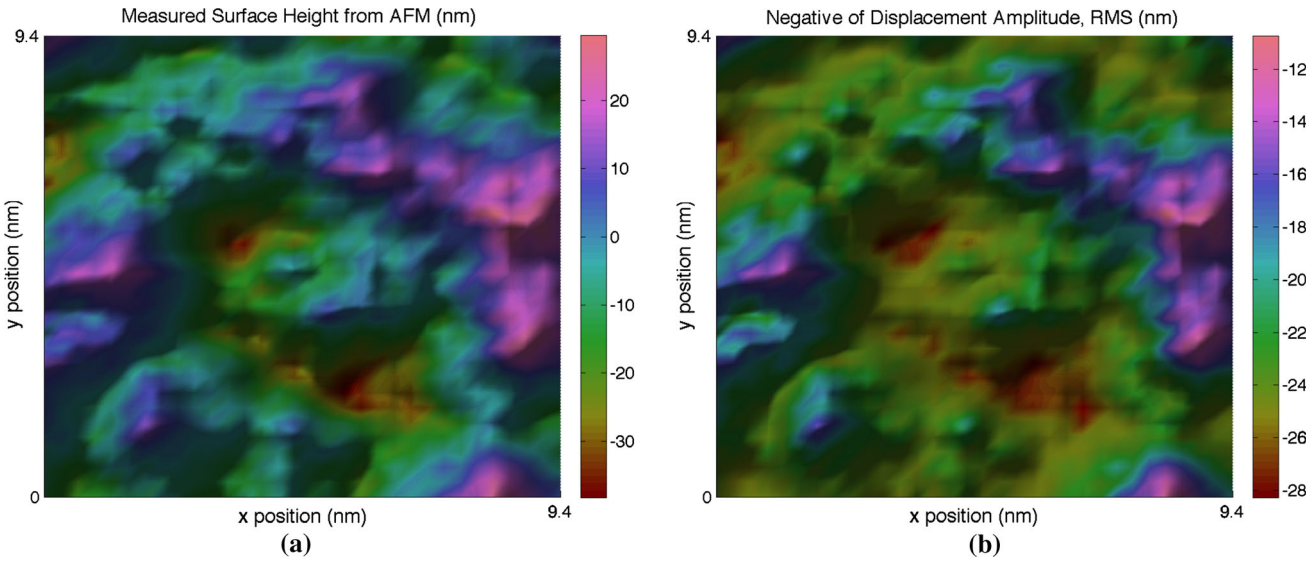

Fig. 17 Selected region of topological surface of a diamond sample: **a** obtained via AFM and **b** reconstructed using cantilever beam tip deflections from numerical simulations

particular point. The simulation was performed for a time span of 3 *ms* considering 1024 time samples. Then, the root-mean-square (RMS) of the time response of the cantilever beam tip was evaluated.

Considering that the closer the tip is to the sample, the smaller should be the tip displacement amplitude; it is proposed that the RMS amplitude could correlate to the measurement point height, as it is observed in what follows. For that, a surface representing the negative of the RMS amplitude of the cantilever tip was plotted and is shown in Fig. 17b. Therefore, the higher the measurement point height, the closer it is to the beam tip, the smaller is the tip displacement amplitude and, thus, the higher is the negative of the RMS amplitude. Indeed, this is what one can notice in Fig. 17b.

A comparison of Fig. 17a, b allows to conclude that they represent a very similar topology, specially in terms of contours with peaks and valleys at the same position. Without a pre-calibration, it is not possible though to infer on the actual heights from the RMS amplitudes. Nevertheless, the numerous similarities allow to obtain a quite good perspective of the original image (surface topology).

5 Conclusions and future works

This work focused on the development and analysis of a parametric model capable of properly representing the dynamics of an AFM cantilever beam when subjected to realistic operation conditions. This was done using a finite element model for the cantilever beam, based on Bernoulli–Euler assumptions, accounting for translational and rotational inertia of the probe tip, on one end (tip), and for the piezoceramic actuator that excites and controls the beam motion, on the other end (base). All material and geometrical properties for the system (cantilever beam, probe tip and piezoceramic actuator) can be parametrized.

Experimental SEM images and frequency responses of a real AFM cantilever beam were used to verify the model and also to define its parameters with very satisfactory results. An analysis of the dynamics of the cantilever beam when subjected to tip-sample nonlinear interaction forces was performed to assess the minimum number of vibration modes to be retained in a reduced-order model. For that, the interaction forces were modeled using Lennard Jones potentials. Using time- and frequency-domain analyses, it was possible to conclude that at least four vibration modes should be retained.

Then, with the help of the proposed reduced model, an analysis of the dynamic response of the cantilever beam for varying tip-sample initial distances was performed. Besides the appearance of the expected nonlinear behavior due to the tip-sample interaction forces, it was observed that the closer the sample is to the beam tip, the smaller is the tip displacement amplitude. Based on this observation, an analysis was performed to assess the correlation between the tip displacement and the surface topology of a diamond sample with satisfactory results.

The analyses presented in this work add value to the understanding and parametrization of an AFM system dynamics, which could help finding better operating conditions for a given system (cantilever beam, probe tip, piezoceramic actuator and sample to be analyzed). Future work will be directed to further studies on the nonlinear

behavior of the system, scale effects on the system dynamics and the inclusion of a positional control law to enable the simulation of realistic operating conditions of AFM systems.

Acknowledgements The authors acknowledge the support of MCT/CNPq/FAPEMIG National Institute of Science and Technology on Smart Structures in Engineering, Grant 574001/2008-5, and the National Council for Scientific and Technological Development (CNPq), Grants 306675/2011-0 and 309193/2014-1. Support of Thin Films Laboratory at the Institute of Physics of University of São Paulo for obtaining images and experimental results is also acknowledged.

References

1. De Oliveira R, Albuquerque D, Cruz T, Yamaji F, Leite F (2012) Measurement of the nanoscale roughness by atomic force microscopy: basic principles and applications, In: Bellitto V (Ed) Atomic force microscopy—imaging, measuring and manipulating surfaces at the atomic scale, Ch. 7. InTech. https://doi.org/10.5772/37583
2. Arantes J (2015) FAPESP Agency - Group investigates physics of surfaces in nanometric scale (in portuguese). http://agencia.fapesp.br/grupo_investiga_a_fisica_de_superficies_em_escala_nanometrica/21194/. Accessed 26 Sept 2016
3. Binnig G, Rohrer H (1983) Scanning tunneling microscopy. Surf Sci 126:236–244
4. Rana MS, Pota HR, Petersen IR (2017) Improvement in the imaging performance of atomic force microscopy: a survey. IEEE Trans Autom Sci Eng 14(2):1265–1285
5. Hansma PK, Schitter G, Fantner GE, Prater C (2006) High-speed atomic force microscopy. Science 314(5799):601–602
6. Dankowicz H (2006) Nonlinear dynamics as an essential tool for non-destructive characterization of soft nanostructures using tapping-mode atomic force microscopy. Philos Trans R Soc A Math Phys Eng Sci 364(1849):3505–3520
7. Misra S, Dankowicz H, Paul MR (2008) Event-driven feedback tracking and control of tapping-mode atomic force microscopy. Proc R Soc A Math Phys Eng Sci 464:2113–2133
8. Nozaki R, Pontes BR Jr, Balthazar JM, Tusset AM (2010) Optimal linear control to an atomic force microscope (AFM) problem with chaotic behavior. In: Proceedings of 9th Brazilian conference on dynamics, control and their applications (DINCON), SBMAC, Serra Negra, SP, pp 371–377
9. Tusset AM, Bueno AM, Nascimento CB, Kaster MS, Balthazar JM (2013) Nonlinear state estimation and control for chaos suppression in MEMS resonator. Shock Vib 20(4):749–761
10. Rodrigues KS, Balthazar JM, Tusset AM, Pontes Jr BR (2011) Dynamical study of a piecewise-smooth model in tapping mode atomic force microscope. In: Proceedings of 10th Brazilian conference of dynamics and their applications (DINCON), SBMAC, Aguas de Lindoia, SP, pp 156–159
11. Jalili N, Laxminarayana K (2004) A review of atomic force microscopy imaging systems: application to molecular metrology and biological sciences. Mechatronics 14(8):907–945
12. Rützel S, Lee SI, Raman A (2003) Nonlinear dynamics of atomic-force-microscope probes driven in Lennard-Jones potentials. Proc R Soc A Math Phys Eng Sci 459:1925–1948
13. Rodrigues KS, Balthazar JM, Tusset AM, Pontes BR Jr, Bueno AM (2014) Preventing chaotic motion in tapping-mode atomic force microscope. J Control Autom Electr Syst 25(6):732–740
14. Stark RW, Schitter G, Stark M, Guckenberger R, Stemmer A (2004) State-space model of freely vibrating and surface-coupled cantilever dynamics in atomic force microscopy. Phys Rev B 69(8):085412
15. Claeyssen JR (2010) The Timoshenko beam model in vibrating AFM cantilevers. In: Proceedings of 9th Brazilian conference on dynamics and their applications (DINCON), SBMAC, Serra Negra, SP, pp 60–70
16. Hsu J-C, Lee H-L, Chang W-J (2007) Flexural vibration frequency of atomic force microscope cantilevers using the Timoshenko beam model. Nanotechnology 18(28):285503
17. Fung R-F, Huang S-C (2001) Dynamic modeling and vibration analysis of the atomic force microscope. J Vib Acoust 123:502–509
18. Georgakaki D, Mitridis S, Sapalidis AA, Mathioulakis E, Polatoglou HM (2013) Calibration of tapping AFM cantilevers and uncertainty estimation: comparison between different methods. Measurement 46:4274–4281
19. Wang B, Wu X, Gan T-H, Rusinek A (2014) Finite element modelling of atomic force microscope cantilever beams with uncertainty in material and dimensional parameters. Eng Trans 62(4):403–421
20. Sajjadi M, Pishkenari HN, Vossoughi G (2017) Dynamic modeling of trolling-mode AFM: Considering effects of cantilever torsion, nanoneedle flexibility and liquid-nanoneedle interactions. Ultramicroscopy 182:99–111
21. Israelachvili JN (2011) Intermolecular and surface forces, 3rd edn. Elsevier Academic Press, New York
22. Nayfeh A, Pai P (2004) Linear and nonlinear structural mechanics. Wiley series in nonlinear science. Wiley, New York
23. Savi MA (2017) Nonlinear Dynamics and Chaos (in portuguese), 2nd edn. E-papers Pub